BBA - Bioenergetics 1862 (2021) 148424

Contents lists available at ScienceDirect

BBA - Bioenergetics

journal homepage: www.elsevier.com/locate/bbabio

Two-dimensional HYSCORE spectroscopy reveals a histidine imidazole as the axial ligand to Chl_{3A} in the $M688H_{PsaA}$ genetic variant of Photosystem I

Michael Gorka [a], Elijah Gruszecki [b], Philip Charles [b], Vidmantas Kalendra [b], K.V. Lakshmi [b,*], John H. Golbeck [a,c,**]

[a] Department of Biochemistry and Molecular Biology, The Pennsylvania State University, State College, PA 16802, USA
[b] Department of Chemistry and Chemical Biology and The Baruch '60 Center for Biochemical Solar Energy Research, Rensselaer Polytechnic Institute, Troy, NY 12180, USA
[c] Department of Chemistry, The Pennsylvania State University, State College, PA 16802, USA

ARTICLE INFO

Keywords:
Photosystem I
Charge separation
Primary acceptor A_0
AMH mutant
2D HYSCORE spectroscopy
Molecular dynamics

ABSTRACT

Recent studies on Photosystem I (PS I) have shown that the six core chlorophyll *a* molecules are highly coupled, allowing for efficient creation and stabilization of the charge-separated state. One area of particular interest is the identity and function of the primary acceptor, A_0, as the factors that influence its ultrafast processes and redox properties are not yet fully elucidated. It was recently shown that A_0 exists as a dimer of the closely-spaced Chl_2/Chl_3 molecules wherein the reduced $A_0^{\bullet-}$ state has an asymmetric distribution of electron spin density that favors Chl_3. Previous experimental work in which this ligand was changed to a hard base (histidine, $M688H_{PsaA}$) revealed severely impacted electron transfer processes at both the A_0 and A_1 acceptors; molecular dynamics simulations further suggested two distinct conformations of PS I in which the His residue coordinates and forms a hydrogen bond to the A_0 and A_1 cofactors, respectively. In this study, we have applied 2D HYSCORE spectroscopy in conjunction with molecular dynamics simulations and density functional theory calculations to the study of the $M688H_{PsaA}$ variant. Analysis of the hyperfine parameters demonstrates that the His imidazole serves as the axial ligand to the central Mg^{2+} ion in Chl_{3A} in the $M688H_{PsaA}$ variant. Although the change in ligand identity does not alter delocalization of electron density over the Chl_2/Chl_3 dimer, a small shift in the asymmetry of delocalization, coupled with the electron withdrawing properties of the ligand, most likely accounts for the inhibition of forward electron transfer in the His-ligated conformation.

1. Introduction

Photosynthetic reaction centers (RC) are multi-subunit membrane protein complexes that carry out light-driven processes of charge separation and stabilization. The light reactions are initiated by the absorption of a photon in highly excitonically-coupled chlorophyll (Chl) molecules located in pigment beds, referred to as the antenna. The photons absorbed from the antenna are transferred to a Chl dimer in the RC, referred to as the primary donor P_X (where X is the wavelength of maximum absorbance) [1,2]. The photoexcitation of P_X results in primary charge separation with a Chl dimer, A_0 [2–4], or (bacterio)pheophytin acceptor, (B)Pheo [5–8], in a Type I or Type II RC, forming the $P_X^{\bullet+}A_0^{\bullet-}$ or $P_X^{\bullet+}$(B)Pheo$^{\bullet-}$ state, respectively. The primary charge-separated state is stabilized by subsequent electron transfer through a series of redox cofactors, ultimately allowing for inter-protein electron transfer through a terminal [4Fe-4S] cluster, F_B, or mobile quinone carrier in a Type I or Type II RC, respectively.

Photosystem I (PS I) is a heterodimeric Type I RC that is well known for its efficient light harvesting and electron transfer reactions (Fig. 1A) (see [2] for a review). Light-driven electron transfer and charge separation in PS I occurs between the primary donor and acceptor, P_{700} and A_0, respectively, that contain a dimer of Chl molecules, $Chl_{1A/1B}$ in P_{700} and $Chl_{2A/2B}$ and $Chl_{3A/3B}$ in $A_{0A/0B}$ (Fig. 1B). It should be noted that the terms A_0 and P_{700} refer to the spectroscopic assignments, while the terms

Abbreviations: 2D HYSCORE, two-dimensional hyperfine sublevel correlation; PS I, Photosystem I; Chl *a*, chlorophyll *a*; DFT, density functional theory.

* Correspondence to: K.V. Lakshmi, Department of Chemistry and Chemical Biology, Rensselaer Polytechnic Institute, Troy, NY 12180, USA.
** Correspondence to: J.H. Golbeck, Departments of Biochemistry and Molecular Biology and Chemistry, The Pennsylvania State University, State College, PA 16802, USA.
E-mail addresses: lakshk@rpi.edu (K.V. Lakshmi), jhg5@psu.edu (J.H. Golbeck).

https://doi.org/10.1016/j.bbabio.2021.148424
Received 1 October 2020; Received in revised form 28 February 2021; Accepted 24 March 2021
Available online 27 March 2021

$Chl_{1A/1B}$, $Chl_{2A/2B}$, and $Chl_{3A/3B}$ are crystallographic assignments. Although there are two active branches of charge transfer, A and B, in PS I, electron transfer along the A-branch has been shown to dominate by a factor of two in cyanobacteria [9–11]. The initial charge-separated state, $P^{\bullet+}_{700}A^{\bullet-}_{0A/0B}$, which is prone to rapid recombination in ~20 ns [11], is stabilized by forward electron transfer through a phylloquinone, $A_{1A/1B}$, and three [4Fe-4S] clusters, F_X, F_A, and F_B (for these cofactors, the spectroscopic and crystallographic assignments are identical). The net result of electron transfer in PS I is the generation of reducing equivalents for storage as NADPH. The high quantum yield of the reaction demonstrates the exquisite tuning of the inter-cofactor distance, relative orientation, and redox potentials of the cofactors, which makes PS I an exemplar for *in vivo* studies on the effects of protein-cofactor interactions on multi-step electron transfer reactions.

We and others have previously demonstrated that the redox properties of the phylloquinone cofactors, $A_{1A/1B}$, are influenced by smart matrix effects of the surrounding protein environment of PS I (see [12] for a review). The determinants of the functional tuning of the A_{1A} and A_{1B} acceptors have been shown to include (i) π-stacking and hydrophobic interactions of $A_{1A/1B}$ with a tryptophan residue ($W697_{PsaA}$/$W677_{psaB}$) that decreases its redox potential [12], (ii) a single hydrogen bond of $A_{1A/1B}$ with a backbone leucine residue $L722_{PsaA}$/$L706_{PsaB}$ that increases its redox potential [12–15], (iii) the presence of the proximal [4Fe-4S] cluster, F_X, that likely assumes multiple conformations that influence electron transfer in different temperature regimes [16], (iv) an asymmetric distribution of proximal water molecules [4], and (v) the orientation of the isoprenoid tail of the phylloquinone molecule [4,17]. However, the factors that influence the primary electron acceptor, A_{0A}/A_{0B}, are less understood and there has been a lack of consensus on its monomeric [18,19] or dimeric nature [20,21] in addition to its overall function in PS I. It has been proposed that $Chl_{3A/3B}$ and $Chl_{2A/2B}$ are involved in the initial charge separation reaction, whereby the hole that was created on $Chl_{2A/2B}$ upon charge separation is re-reduced by the primary donor, P_{700} [22–25]. In contrast, there have been proposals that involve the formation of a highly-coupled exciplex among all six Chl molecules in the core of PS I ($Chl_{1A/1B}$, $Chl_{2A/2B}$, and $Chl_{3A/3B}$) that serve to provide the favorable downhill energetics and spatial separation of charges that are essential for effective charge stabilization in PS I [26,27]. Recent research carried out by our laboratory has provided direct experimental evidence that the $A^{\bullet-}_{0A}$ state indeed consists of a dimer of Chl_{2A} and Chl_{3A} [28]. This work supported previous spectroscopic observations [20] and semi-continuum calculations [21] and suggested asymmetric electron density distribution on Chl_{2A} and Chl_{3A}, albeit in favor of Chl_{3A}. Dimerization therefore appears to be an effective strategy for tuning the redox properties of the early Chl cofactors.

However, there remain unanswered questions on an unusual property of A_0, namely, the nature and significance of the axial ligand to $Chl_{3A/3B}$. The high-resolution X-ray crystal structure of cyanobacterial PS I has revealed surprising features of the Chl cofactors ($Chl_{1A/1B}$, $Chl_{2A/2B}$ and $Chl_{3A/3B}$ in Fig. 1B) in the PsaA and PsaB core of polypeptides [3,4]. While the Mg^{2+} ion of $Chl_{1A/1B}$ is axially coordinated by a nitrogen ligand from a histidine residue ($H680_{PsaA}$ and $H660_{PsaB}$) and $Chl_{2A/2B}$ has an axial oxygen ligand from a water molecule, $Chl_{3A/3B}$ is axially coordinated by a soft base sulfur ligand from a methionine residue ($M688_{PsaA}$ and $M668_{PsaB}$) [4]. This is highly unusual and is contrary to hard-soft acid-base theory [29] where the relatively hard Mg^{2+} ion in $Chl_{3A/3B}$ is expected to be coordinated by a hard base, such as a nitrogen atom of a histidine or an oxygen atom of water, rather than a soft sulfur atom of a methionine residue ($M688_{PsaA}$ and $M668_{PsaB}$) [4]. This suggests that the axial coordination of the central Mg^{2+} ion of $Chl_{3A/3B}$ could be instrumental in achieving a low mid-point potential that is necessary for establishing rapid and efficient charge separation with the primary donor, P_{700} [30].

Previous studies have examined genetic variants of the $M688_{PsaA}$ and $M668_{PsaB}$ residue in both *Chlamydonomas reinhardtii* [31–36] and *Synechocycstis* sp. PCC 6803 [37–41] to understand better the role of the soft base sulfur ligand in the tuning of the $Chl_{3A/3B}$ cofactor of $A_{0A/0B}$. In particular, the results obtained from the variants where the $M688_{PsaA}$ or $M668_{PsaB}$ residue was replaced by Leu, Asn, and His have been notable [37–41]. The $M688H_{PsaA}$ and $M668H_{PsaB}$ variants (where $M688_{PsaA}$ or $M668_{PsaB}$ was replaced by His) showed the most significant changes in the rates and efficiency of electron transfer in comparison with WT PS I. Using ultrafast time-resolved (TR) optical spectroscopy, it was demonstrated that the formation of the initial charge-separated state, $P^{\bullet+}_{700}A^{\bullet-}_{0}$, was not affected by the replacement of $M688_{PsaA}$ or $M668_{PsaB}$ by a His residue [9]. However, the subsequent electron transfer steps that stabilize charge separation were affected in the $M688H_{PsaA}$ and $M668H_{PsaB}$ variants. The TR optical spectra with a time delay of 500 ps revealed spectral features from a mixed population of $P^{\bullet+}_{700}A^{\bullet-}_{0}$ and $P^{\bullet+}_{700}A^{\bullet-}_{1}$, implying severely impacted electron transfer from the $A^{\bullet-}_{0}$ state to the A_1

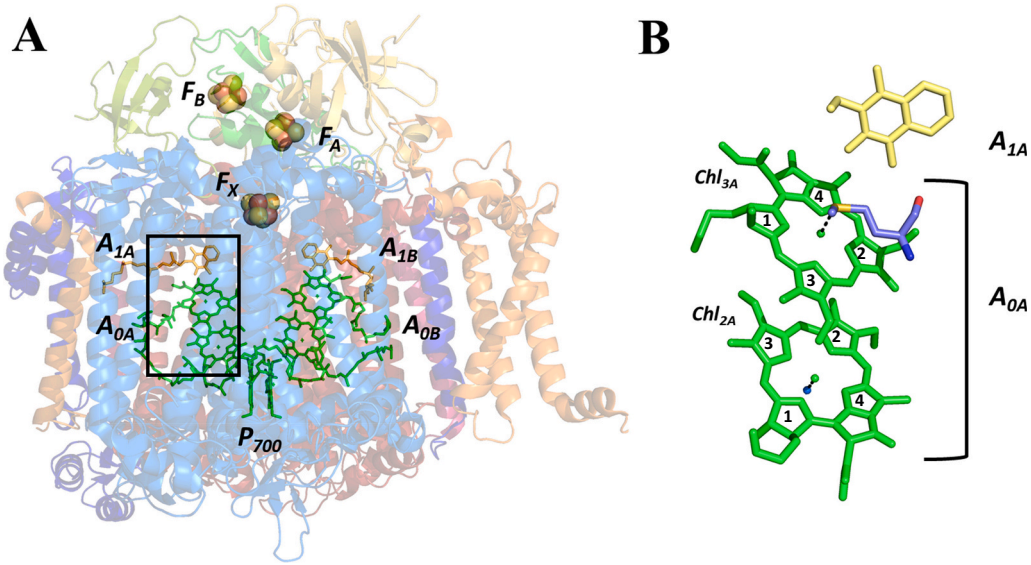

Fig. 1. (A) Electron-transfer chain depicting the primary donor ($Chl_{1A/1B}$), acceptors ($Chl_{2A/2B}$, $Chl_{3A/3B}$, $A_{1A/1B}$, F_X, F_A and F_B) superimposed on the major polypeptide subunits of PS I, and (B) the binding site of the primary acceptors, $Chl_{2A/3A}$ and A_{1A} as observed in the 2.5 Å crystal structure of PS I with truncated tails on the Chl and phylloquinone molecules [4].

cofactor in the affected branch. Both M688H$_{PsaA}$ and M668H$_{PsaB}$ had yielded biphasic kinetics, where the rate of electron transfer in the A- and B-branch decreased to 150 ps and 250 ps, respectively, while the unaffected complementary branch remained at 26 ps. Additionally, there was a sub-population of each variant that displayed complete inhibition of forward electron transfer that occurred in 27% and 7% of the A- and B-branch variant, respectively [9]. In contrast, wild-type PS I consistently displayed monophasic and quantitative formation of $P^{\bullet+}_{700}A^{\bullet-}_{1}$ with a lifetime of 26 ps.

These observations on the M688H$_{PsaA}$ and M668H$_{PsaB}$ variants of PS I were further corroborated by transient EPR and TR optical spectroscopy [9]. The signal of the spin correlated radical pair ($P^{\bullet+}_{700}A^{\bullet-}_{1A}$) in each variant that was detected by transient EPR spectroscopy showed qualitative similarities to WT PS I, but contained an additional signal from the $P^{\bullet+}_{700}A^{\bullet-}_{0}$ recombination triplet that occurred from the affected branch [9]. Moreover, in agreement with the TR spectroscopy measurements that showed less inhibition in the B-branch, the triplet was smaller for the variant in the B-branch than the A-branch [9]. Detailed information on electron transfer was obtained by TR optical spectroscopy in the ns – s time regime where measurements at 480 nm were used to monitor the electrochromic shift of a nearby carotenoid that served as a proxy for the re-oxidation of $A^{\bullet-}_{1}$ [42]. The TR optical measurements showed charge recombination between $A^{\bullet-}_{1}$ and $P^{\bullet+}_{700}$ instead of forward transfer from $A^{\bullet-}_{1}$ to F_X, implying that forward transfer was completely inhibited in the affected branch. The reduction of $P^{\bullet+}_{700}$ was also monitored at 820 nm and the results indicated that there was recombination from both $A^{\bullet-}_{0}$ and $A^{\bullet-}_{1}$ in the affected branch of both variants of PS I [9].

Based on these observations, it has been proposed that the His residue in the M688H$_{PsaA}$ variant functions in two states with approximately equal populations. The first allows it to serve as the axial ligand to Chl$_{3A}$, resulting in a sufficiently raised redox potential to inhibit forward electron transfer from A$_{0A}$ to the A$_{1A}$ phylloquinone. The second conformation allows the His residue to provide a hydrogen bond to the carbonyl of the A$_{1A}$ phylloquinone. This state allows forward electron transfer from A$_{0A}$ to A$_{1A}$ (albeit slowed by a factor of ~6), however, the hydrogen bond raises the redox potential of A$_{1A}$ such that electron transfer from A$_{1A}$ to F_X is unfavorable. Previous molecular mechanics calculations had supported this proposal as two separate conformers were observed, one conformation with the ε-nitrogen of the His at a distance of ~2.3 Å from the central Mg^{2+} ion of Chl$_{3A}$, and a separate conformer with the δ-nitrogen of the His at an average distance of 3.4 Å from the C1 carbonyl carbon atom of the A$_1$ phylloquinone [9].

However, to date there is a lack of direct experimental evidence that the ε-nitrogen atom of the His residue in M688H$_{PsaA}$ PS I is axially coordinated at the central Mg^{2+} ion of Chl$_{3A}$ in the $A^{\bullet-}_{0A}$ state. Two-dimensional (2D) hyperfine sublevel correlation (HYSCORE) and other pulsed EPR techniques have previously afforded extensive information on the electronic structure of various cofactors of PS I [13–15,43–46] as well as RCs from other organisms [47–50]. In the present study, we employ 2D HYSCORE spectroscopy in conjunction with DFT calculations to provide unambiguous evidence that the His residue in the M688H$_{PsaA}$ variant of PS I does indeed serve as an axial ligand to the Chl$_{3A}$ cofactor. Most interestingly, the replacement of the axial ligand of Chl$_{3A}$ does not appear to disrupt electron delocalization over the Chl$_{2A/2B}$ and Chl$_{3A/3B}$ cofactors in the $A^{\bullet-}_{0}$ state of PS I.

2. Materials and methods

2.1. Preparation of the M688H$_{PsaA}$ variant of Photosystem I

Growth and purification of PS I form the M688H$_{PsaA}$ variant was performed in accordance with previously published methods [9,37]. The Quick Change site-directed mutagenesis kit (Stratagene Inc.) was used to introduce the desired point mutation into the pIBC plasmid. The mutated pIBC plasmid was used to transform the pWX3 recipient strain to generate the M688H$_{PsaA}$ variant. Transformants were selected and segregated under low light intensities with increasing chloramphenicol concentration from 5 μg/mL to 50 μg/mL. DNA fragments containing the mutation sites were amplified by PCR from genomic DNA of the variant cells and were sequenced to confirm full segregation and the desired nucleotide change. Preparation of thylakoid membranes and isolation of PS I trimers was performed using a non-ionic detergent n-dodecyl β-D-maltopyranoside (β-DDM) according to previously published procedures [51].

2.2. Cryogenic trapping of the $A^{\bullet-}_{0}$ state of M688H$_{PsaA}$ Photosystem I

The M688H$_{PsaA}$ variant of PS I was loaded in a 4 mm quartz EPR tube (Wilmad LabGlass, SP Scienceware, Vineland, NJ) and cooled in a dewar containing a dry ice/ethanol mixture at 220 K for 2 min in the dark. After equilibration at 220 K, the sample was illuminated for 1 min with 100 W of white light and rapidly frozen in the dark in liquid nitrogen at 77 K after illumination.

2.3. Pulsed electron paramagnetic resonance spectroscopy

The EPR spectra were obtained on a custom-built continuous-wave (*cw*)/pulsed X-band Bruker Elexsys 580 EPR spectrometer using a dielectric flex-line ER 4118-MD5 probe (Bruker BioSpin, Billerica, MA) and a dynamic continuous-flow cryostat CF935 (Oxford Instruments, Oxfordshire, U.K.). The 2D HYSCORE spectra and magnetic field-sweep electron-spin-echo (FS-ESE) spectrum were acquired at 80 K and 30 K, respectively. The 2D HYSCORE spectra were obtained at a magnetic field position of 345.8 mT.

For the 2D ^{1}H and ^{14}N HYSCORE spectra of the $A^{\bullet-}_{0A}$ state of the M688H$_{PsaA}$ variant of PS I, the echo amplitude was measured using the pulse sequence ($\pi/2$–τ–$\pi/2$–t_1–π–t_2–$\pi/2$–τ–echo) with a τ value of 136 ns, and a 16 ns detector gate. The pulse length was 8 ns and 16 ns for the $\pi/2$- and π-pulse, respectively. The delays in the pulse sequence are defined as the difference in the starting point of the pulses. The echo intensity was measured as a function of t_1 and t_2, where t_1 and t_2 were incremented in steps of 16 ns from an initial value of 40 ns and 32 ns, respectively. A total of 384 steps were used for each dimension. The 8 ns time difference between the initial value of t_1 and t_2 was set to account for the difference in length between the $\pi/2$- and π-pulse. This provided symmetric spectra in both dimensions. The unwanted echoes were eliminated by applying a 16-step phase cycling procedure. In a 2D HYSCORE experiment, the presence of possible pulse imperfections could result in the appearance of unwanted peaks along the diagonal due to incomplete excitation by the third microwave pulse of the 2D HYSCORE pulse sequence. In this study, we performed additional 2D HYSCORE measurements in the absence of the third pulse and used difference spectroscopy to eliminate the three-pulse ESEEM contributions along the diagonal (Fig. 2A, C). This does not affect the overall results or interpretation as the hyperfine couplings with the $N^A - N^D$ nitrogen atoms of the $A^{\bullet-}_{0A}$ state give rise to off-diagonal cross-peaks in the (−,+) and (+,+) quadrant.

The time domain 2D HYSCORE data was processed using MATLAB R2018b. A third order polynomial baseline was subtracted from the resulting time-domain spectra. The corrected spectra were zero-filled to obtain [2048 × 2048] matrix and Fourier transformed using a Fast Fourier Transformation (FFT) algorithm. The frequency domain spectra were plotted as the amplitude (absolute value) of the 2D frequency components.

Numerical simulations of the experimental 2D HYSCORE spectra using the hyperfine parameters obtained from the spectra analysis were performed using the "saffron" function of the EasySpin software package [52].

2.4. Density functional theory calculations

DFT calculations of the $A^{\bullet-}_{0}$ state of the M688H$_{PsaA}$ variant of PS I

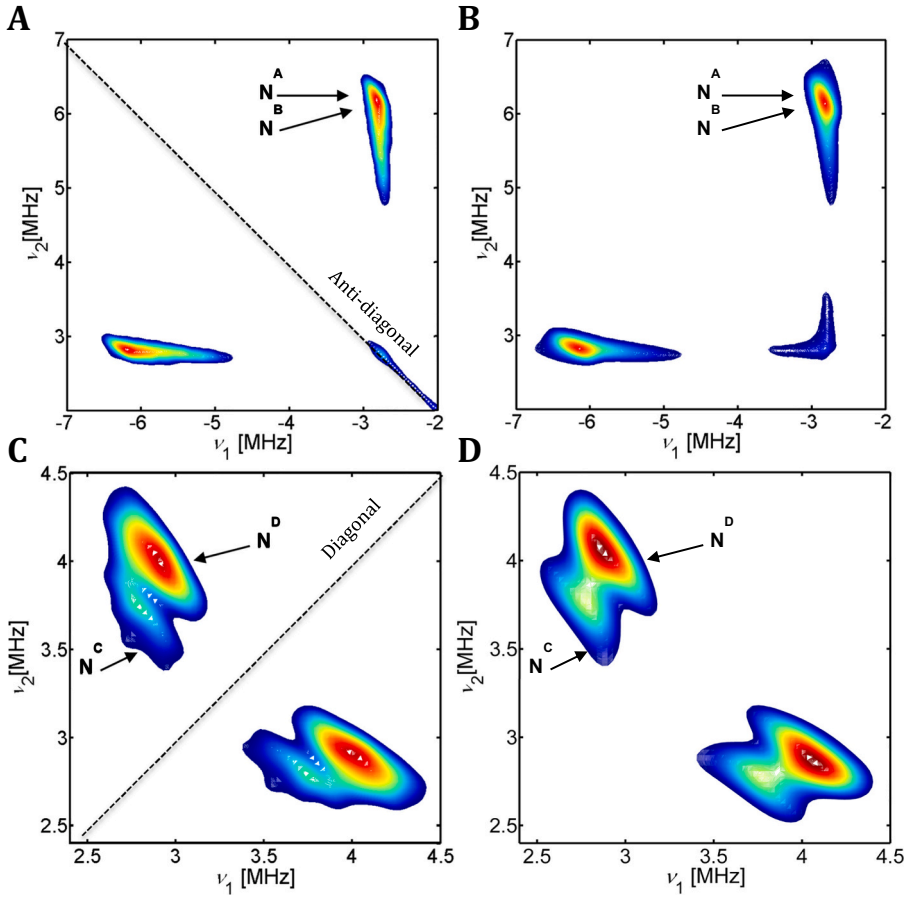

Fig. 2. (A, C) Experimental and (B, D) simulated 2D ^{14}N HYSCORE spectra of the $A_{0A}^{\bullet-}$ state of the M688H$_{PsaA}$ variant of PS I. The cross-peaks in the (−,+) and (+,+) quadrant arise from the hyperfine interactions of the unpaired electron spin with four nitrogen-14 atoms (nuclear spin, I = 1), N^A – N^D. The experimental spectrum was acquired at 80 K.

were performed at the B3LYP level of theory with a def2-SVP basis set using the software ORCA 4.0 [53,54]. The calculations employed the RIJCOSX approximation in conjunction with the CPCM solvent model using a dielectric (ε) of 4.0 to approximate the surrounding protein environment [50]. The charge and electron spin density distribution in the highest occupied and singly occupied molecular orbital (HOMO and SOMO, respectively) that were obtained from the DFT calculations was visualized using the software package, Visual Molecular Dynamics (VMD) [55]. The hyperfine and quadrupolar couplings for the magnetically-coupled nitrogen atoms were calculated as described above on the optimized computational models using the EPR-II basis set for the lighter atoms and the 6-31G(d) basis set for the Mg^{2+} ions. The initial coordinates for the computational models were derived from the X-ray crystal structure of wild-type (WT) PS I from *Thermosynechococcus elongatus* (PDB ID: 4JB0) [4] and the M688H$_{PsaA}$ variant was introduced into the structure using PyMOL (Schrodinger, Inc.) with the His residue mono-protonated on the δ-nitrogen. The structure of the M688H$_{PsaA}$ variant was optimized as previously described [9] and the energy of the individual conformers were optimized and analyzed to yield histograms of interatomic distances. The minimum energy structure(s) with a favorable distance between the axial H688$_{PsaA}$ nitrogen ligand to the Mg^{2+} ion of Chl$_{3A}$ were used as a starting point for optimization of the DFT models. The DFT calculations were performed on five computational models with increasing levels of complexity that ranged from 89 to 333 atoms in size. The $Chl_{3A}^{\bullet-}$ anion with H688$_{PsaA}$ was used as a starting point and A_{1A}, Chl$_{2A}$, and its water ligand were included in subsequent models.

3. Results

3.1. Field-sweep electron-spin-echo (FS-ESE) spectroscopy of the $A_0^{\bullet-}$ state in the M688H$_{PsaA}$ variant

Cryogenic white light illumination of the M688H$_{PsaA}$ variant of PS I for 1 min at 220 K resulted in the photoaccumulation of the reduced primary acceptor, $A_{0A}^{\bullet-}$. The $A_0^{\bullet-}$ state is paramagnetic with an unpaired electron spin (S = ½) that results in the observation of a FS-ESE signal at a *g*-value of 2.0052 (Fig. 1S) with a peak-to-peak line width of 1.28–1.51 mT. Photoaccumulation of $A_0^{\bullet-}$ is only possible in RCs where forward electron transfer to A_1 is blocked, normally accomplished by removal of the A_1 phylloquinone and reduction of the FeS clusters. However, ~ 50% of electrons that reach A_{0A} are blocked from forward electron transfer in the M688H$_{PsaA}$ variant, from the conformer where the His688$_{PsaA}$ residue is ligating Chl$_{3A}$ [9]. Since this affect is branch specific, it ensured that the spectra only contained signals from the $A_{0A}^{\bullet-}$ and, lacked any contribution from $A_{0B}^{\bullet-}$.

3.2. 2D ^{14}N HYSCORE spectroscopy of the $A_{0A}^{\bullet-}$ state in the M688H$_{PsaA}$ variant

Although we observed the characteristic FS-ESE signal of the $A_{0A}^{\bullet-}$ state in the M688H$_{PsaA}$ variant of PS I in Fig. 1S, the weak electron-nuclear hyperfine interactions of the unpaired electron spin of $A_{0A}^{\bullet-}$ with neighboring magnetic nuclei, such as, nitrogen-14 (^{14}N) and hydrogen (^{1}H) atoms are obscured in the spectrum due to inhomogeneous line broadening. However, these weak hyperfine interactions with

the surrounding magnetic nuclei can be detected by the application of advanced pulsed EPR spectroscopy methods [56–58] such as electron nuclear double resonance (ENDOR) [59–61] and electron spin echo envelope modulation (ESEEM) spectroscopy that are designed to overcome this problem [62,63]. Nevertheless, it is a major challenge to interpret the experimental data that are obtained by ENDOR and ESEEM spectroscopy as these methods simultaneously detect the presence of multiple nuclei in the vicinity of the paramagnetic center, which results in severe overlap of spectral features from the different nuclei. In comparison with one-dimensional (1D) EPR spectroscopy methods, the use of two-dimensional (2D) methods, such as hyperfine sub-level correlation (HYSCORE) spectroscopy, simplifies the detection and analysis of multiple electron–nuclear interactions. This is because in 2D HYSCORE spectroscopy, the overlapping nuclear frequencies are separated in a second dimension and there is a correlation of nuclear frequencies that arise from different electron spin manifolds [64]. The enhanced resolution of 2D HYSCORE spectroscopy with respect to simultaneous detection of multiple nuclei provides significant advantages for the study of paramagnetic centers such as the $A_{0A}^{\bullet-}$ state of PS I. Indeed, previous work has demonstrated the successful application of 2D HYSCORE spectroscopy to determine the electronic structure of charge-transfer cofactors in both Type I and Type II RCs [15,50,65–68].

Shown in Fig. 2S is the complete 2D HYSCORE spectrum of the $A_{0A}^{\bullet-}$ state of the M688H$_{PsaA}$ variant of PS I. The spectrum was measured at the magnetic field position corresponding to the maximum of the field-sweep EPR spectrum (345.8 mT) in Fig. 1S and is comprised of two distinct groups of cross-peaks. The first group of cross-peaks consists of two pairs of pronounced peaks in the (−,+) and (+,+) quadrant of the spectrum that are centered at multiples of the ^{14}N Zeeman frequency of 1.07 MHz. These peaks arise from electron-nuclear hyperfine interactions of the unpaired electron spin (S = ½) of the $A_{0A}^{\bullet-}$ state with the constituent ^{14}N atoms (nuclear spin of I = 1). The second pair of cross-peaks are centered at the ^{1}H Zeeman frequency of 14.7 MHz in the (+,+) quadrant of the spectrum that are due to the hyperfine interactions with multiple hydrogen atoms (nuclear spin of I = ½) that are interacting with the unpaired electron spin of the $A_{0A}^{\bullet-}$ state.

Shown in Fig. 2A–D are the experimental and simulated 2D ^{14}N HYSCORE spectra of the $A_{0A}^{\bullet-}$ state of the M688H$_{PsaA}$ variant of PS I that displayed cross-peaks in both (−,+) and (+,+) quadrant of the spectrum. Typically, the spectral features arising from ^{14}N nuclei that are strongly hyperfine-coupled to the unpaired electron spin lead to cross-peaks in the (−,+) quadrant, and cross-peaks from weakly-coupled nuclei are observed in the (+,+) quadrant [64]. Thus, the two pairs of well-pronounced and intense overlapping cross-peaks at (−6.2, 2.8) MHz that are symmetrically displaced from the main anti-diagonal in the (−,+) quadrant of the spectrum (Fig. 2A, B) are identified as double quantum (DQ) correlations of ^{14}N atoms (termed N^{A} and N^{B}) that are strongly coupled to the unpaired electron spin (S = ½) of $A_{0A}^{\bullet-}$. The separation between the cross-peaks is nearly four times the corresponding ^{14}N Zeeman frequency (ν_N of 1.07 MHz). In contrast, there are two overlapping pairs of cross peaks at a frequency of (2.75, 3.7) MHz and (2.85, 4.0) MHz in the (+,+) quadrant of the spectra in Fig. 2C, D that are symmetric about the main diagonal that arise from weakly hyperfine-coupled ^{14}N atom(s), N^{C} and N^{D}. In each case, the small shift along the diagonal from multiples of the ^{14}N Zeeman frequency, ν_N, is due to the nuclear quadrupolar interaction of the nitrogen atoms.

It is necessary to determine the hyperfine and quadrupolar parameters in order to identify the nitrogen atoms that are magnetically interacting with the unpaired electron spin of the $A_{0A}^{\bullet-}$ state. The observation of well-defined cross-peaks in the experimental 2D ^{14}N HYSCORE spectrum of the $A_{0A}^{\bullet-}$ state in Fig. 2A and C facilitate quantitative determination of the value of the isotropic hyperfine coupling constant, A_{iso}, quadrupolar coupling constant, K, and asymmetry parameter, η, for each of the nitrogen atoms, N^{A} – N^{D} (Table 1). The quadrupole interaction is determined by electric field gradients that are experienced by the nucleus when the nuclear spin I > 1/2. The quadrupolar tensor parameters,

Table 1
Experimental ^{14}N isotropic hyperfine (A_{iso}), quadrupolar (K) and asymmetry (η) parameters of the $A_{0A}^{\bullet-}$ state of the M688H$_{PsaA}$ variant of PS I obtained from the 2D ^{14}N HYSCORE spectroscopy measurements.

Nitrogen	A_x [MHz]	A_y [MHz]	A_z [MHz]	A_{iso} [MHz]	K	η
N^{A}	3.7 ± 0.2	1.0 ± 0.2	3.7 ± 0.2	2.80 ± 0.2	0.69 ± 0.02	0.5 ± 0.2
N^{B}	3.6 ± 0.2	1.0 ± 0.2	3.6 ± 0.2	2.73 ± 0.2	0.69 ± 0.02	0.5 ± 0.2
N^{C}	0.1 ± 0.2	0.1 ± 0.2	1.5 ± 0.2	0.57 ± 0.2	0.69 ± 0.02	0.4 ± 0.2
N^{D}	0.4 ± 0.2	0.4 ± 0.2	1.2 ± 0.2	0.67 ± 0.2	0.744 ± 0.02	0.5 ± 0.2

K and η, where $K = e^2qQ / 4\hbar$, reflect the size and asymmetry of the electric field gradient at the position of the nucleus and is directly related to the chemical environment of the hyperfine-coupled nucleus. Hence, these parameters can be used to identify the type of chemical bonding of the nucleus. For the nitrogen atoms N^{A} – N^{C}, the quadrupolar parameter, K, is identical with a value of 0.69 MHz. This indicates the similar chemical nature of the N^{A} – N^{C} nitrogen atoms. Based on the K value of 0.69 ± 0.02 MHz for N^{A} – N^{C}, we assign these nitrogen atoms to the pyrrole ring(s) of the Chl molecules that constitute the $A_{0A}^{\bullet-}$ state [50,56,69,70]. In contrast, the K value of 0.74 ± 0.02 MHz for the nitrogen atom, N^{D}, in Table 1 suggests that this is an imino nitrogen atom of a histidine residue that is axially coordinated to the central Mg^{2+} ion of a Chl ring. The value of $e^2qQ/\hbar$ for an uncoordinated imino ^{14}N atom of an imidazole group has been reported to be ~3.3 ± 0.3 MHz [66,71]. However, upon coordination with a metal ion this value is reduced to ~2.0–3.0 MHz, which corresponds to a value of 0.50–0.75 MHz for K (66, 71). The observed quadrupolar constant, K, of 0.74 for N^{D} is well within this range of values and is therefore assigned to the imino nitrogen of a histidine residue axially coordinated to a Chl molecule in the $A_{0A}^{\bullet-}$ state. Taken together, the quadrupolar couplings, K, indicate that N^{A} – N^{C} are a part of the Chl ring(s) and N^{D} belongs to the His residue that is coordinated to the $A_{0A}^{\bullet-}$ state in the M688H$_{PsaA}$ variant of PS I. This is in agreement with previous observations that a histidine residue is axially coordinated to the central Mg^{2+} ion of the primary donor Chl *a*/Chl *a*′ heterodimer and BChl *a*′ dimer of PS I and bRC from purple bacteria, respectively [43,44,72].

In contrast to the similar value of the quadrupolar coupling constants that were observed for N^{A} – N^{C}, the isotropic component of the hyperfine interaction, A_{iso}, of 2.8 MHz and 2.73 MHz for N^{A} and N^{B} is approximately five times the A_{iso} value of N^{C}, 0.57 MHz. The isotropic component, or Fermi contact term, of the hyperfine interaction results from the exchange polarization of electrons which results in the presence of finite electron spin density at the nucleus. This indicates a large asymmetry in the electron spin density that is localized on each of these nitrogen atoms, N^{A} – N^{C}. Interestingly, the A_{iso} for all three nitrogens, N^{A} – N^{C}, is smaller than A_{iso} values of the hyperfine-coupled nitrogen atoms that were previously observed in the monomeric Chl $a^{\bullet-}$ anion or Chl $a^{\bullet+}$ cation *in vitro* [1,46,73–75]. Moreover, this value is in agreement with the values that were recorded for the primary donor cation, $P_{700}^{\bullet+}$ [1,72], and the $A_0^{\bullet-}$ state of WT PS I [28]. The smaller hyperfine coupling constants for the N^{A} – N^{C} nitrogen atoms indicate that the unpaired electron spin is delocalized over two or more Chl rings in the $A_0^{\bullet-}$ state of the M688H$_{PsaA}$ variant of PS I. However, these results do not identify the specific Chl molecules that are involved in the charge delocalization. The A_{iso} value for N^{D}, a feature not seen in WT PS I, is 0.67 MHz, showing a finite but small amount of electron density residing on the imino nitrogen of the H688$_{PsaA}$ residue.

3.3. Density functional theory calculations of the $A_0^{\bullet-}$ state of the $M688H_{PsaA}$ variant

We performed DFT calculations that complement the experimental 2D ^{14}N HYSCORE spectroscopy measurements in the previous section to understand better the electronic structure of the $A_{0A}^{\bullet-}$ state of the $M688H_{PsaA}$ variant of PS I. As described in the Materials and methods section, in the absence of an X-ray crystal structure for the $M688H_{PsaA}$ variant, the coordinates for the computational models for the DFT calculations were derived from the 2.5 Å resolution X-ray crystal structure of WT PS I from *T. elongatus* [4]. The $M688_{PsaA}$ residue in the WT PS I structure was replaced by a His residue and energy minimization was performed on the resulting variant (Fig. 3A–B) [9]. The minimum energy structures were analyzed to construct a histogram of the distance between the imino nitrogen of $H688_{PsaA}$ to the Mg^{2+} ion of the Chl_{3A} molecule and the structures with the most favorable metal-to-ligand distances were selected for further optimization using DFT methods. We used the results of the DFT calculations on an isolated $Chl_{3A}^{\bullet-}$ anion as a test case to reproduce the electron spin delocalization over a monomeric Chl $a^{\bullet-}$ anion (Fig. 5S). The electron spin density distribution in the singly occupied molecular orbital (SOMO) of the computational model with an isolated $Chl_{3A}^{\bullet-}$ anion reproduced the trends that were previously observed for Chl $a^{\bullet-}$ anions *in vitro* [3,76].

Subsequently, we expanded the computational model to include both the Chl_{3A} and Chl_{2A} molecules with their axial ligands, $H688_{PsaA}$ and water, respectively, as well as the A_{1A} quinone acceptor. Previous computational studies of proteins have used quantum mechanics/molecular modeling (QM/MM), which involves intensive quantum mechanical calculations on a small group of selected atoms, while classical mechanics are used for the rest of the system. However, the electronic coupling between the Chl rings in the present case would likely complicate the use of hybrid methods. Recent studies by Pantazis and coworkers [77] on highly-coupled Chl and pheophytin molecules in Photosystem II (PS II) suggests that future refinement of this system using QM/MM methods is possible. In this study, we used an all-quantum mechanical approach to model the electronic structure of the cofactors as a whole. We observed that the electron spin density distribution in the SOMO of the computational model containing the Chl_{3A} and Chl_{2A} molecules with the respective axial ligands, and the A_{1A} quinone acceptor was delocalized on Chl_{3A} and Chl_{2A} rings in the $A_{0A}^{\bullet-}$ state (Fig. 4A). This is consistent with the smaller ^{14}N hyperfine coupling constants that were observed for the ring nitrogen atoms, $N^A - N^C$, in the 2D ^{14}N HYSCORE spectroscopy measurements. This delocalization is similar to that observed for WT PS I examined under the same parameters (Fig. 4B), with the notable exception that more electron density resides on Chl_{3A} in WT PS I.

A comparison of the experimental ^{14}N hyperfine coupling constants with the couplings that were calculated by DFT methods indicates that the hyperfine-coupled N^A and N^B nitrogen atoms in the 2D HYSCORE measurements correspond to the nitrogen atoms at the N^1 and N^3 of Chl_{2A} and N^C matches the N^2 atom of Chl_{3A} in the computational model of the $A_{0A}^{\bullet-}$ state of the $M688H_{PsaA}$ variant of PS I (using the numbering scheme for pyrrole nitrogen atoms as depicted in Fig. 1) (Table 2S). However, the DFT calculations predict hyperfine couplings of 1.33–1.55 MHz with the N^1 and N^3 atom on Chl_{3A} and N^2 on Chl_{2A}. The hyperfine signals from these nitrogen atoms were not detected in the 2D ^{14}N HYSCORE experiments. Numerical simulations indicate that the cross-peaks arising from pyrrole nitrogen atoms with hyperfine couplings of 1.3–1.4 MHz are close to the signals from N^C but they may be diminished in intensity due to cross-suppression effects from the strongly hyperfine coupled N^1 and N^3 atoms of Chl_{2A} [78,79]. The resolution of the hyperfine signals of the N^3 and N^1 atoms on Chl_{3A} and N^2 on Chl_{2A} will be the focus of future studies. The larger magnitude of the hyperfine coupling, A_{iso}, of N^1 and N^3 of Chl_{2A} is in agreement with the increased electron spin density on Chl_{2A} in the $M688H_{PsaA}$ variant, which is in contrast with WT PS I (Fig. 4A–B) [28]. Interestingly, the DFT calculations reveal a hyperfine and quadrupolar coupling value of 0.45 MHz and 0.85 MHz, respectively, for the nitrogen atom N^D of $His688_{PsaA}$ that is an axial ligand to the Mg^{2+} ion of the Chl_{3A} ring. These couplings are close to the experimental A_{iso} and K values of 0.67 ± 0.2 MHz and 0.74 MHz that were obtained by 2D HYSCORE spectroscopy.

4. Discussion

The two most informative parameters obtained from 2D HYSCORE spectroscopy measurements of the $A_{0A}^{\bullet-}$ state of the $M688H_{PsaA}$ variant of PS I are the isotropic hyperfine coupling constant or Fermi contact term, A_{iso}, and the quadrupolar coupling constant, K. The isotropic hyperfine coupling, A_{iso}, is directly related to the extent of the electron spin density distribution in a paramagnetic species [80]. We have determined that the A_{iso} values of the ^{14}N hyperfine interactions in the $A_0^{\bullet-}$ state of WT PS I range from 0.52–2.80 MHz [28], and are smaller than the analogous ^{14}N A_{iso} values that were obtained for a monomeric Chl $a^{\bullet+}$ cation [1,73,75,81] and $^{\bullet}$ anion [74] *in vitro* (4.40–5.50 MHz). However, the A_{iso} values of the ^{14}N atoms for the $A_{0A}^{\bullet-}$ state were comparable in magnitude to known Chl *a* dimers, such as the primary donor cation of PS I, $P_{700}^{\bullet+}$, that range from 1.37–2.80 MHz [28]. This provided the best evidence that the electron spin density in the $A_0^{\bullet-}$ state is distributed over a dimer of Chl molecules, $Chl_{2A/2B}$ and $Chl_{3A/3B}$ of WT PS I.

The isotropic hyperfine couplings, A_{iso}, of the pyrrole nitrogen atoms in the $A_{0A}^{\bullet-}$ state of the $M688H_{PsaA}$ variant of PS I are in the range of 0.57–2.80 MHz. There is, however, a major difference between the WT and $M688H_{PsaA}$ variant in the present study. While the axial ligand of Chl_{3A} is the $M688_{PsaA}$ residue in WT PS I, it has been replaced by a His residue in the $M688H_{PsaA}$ variant. However, it was unclear whether the His residue would ligate the Mg^{2+} ion of Chl_{3A} and if so, whether it would result in a change in the electronic properties of Chl_{3A} in a way that could impact the electron spin delocalization over the Chl dimer in the $A_{0A}^{\bullet-}$ state. Upon comparison of the 2D ^{14}N HYSCORE spectra of the $A_0^{\bullet-}$ state of WT and $M688H_{PsaA}$ PS I, we observed an additional cross-

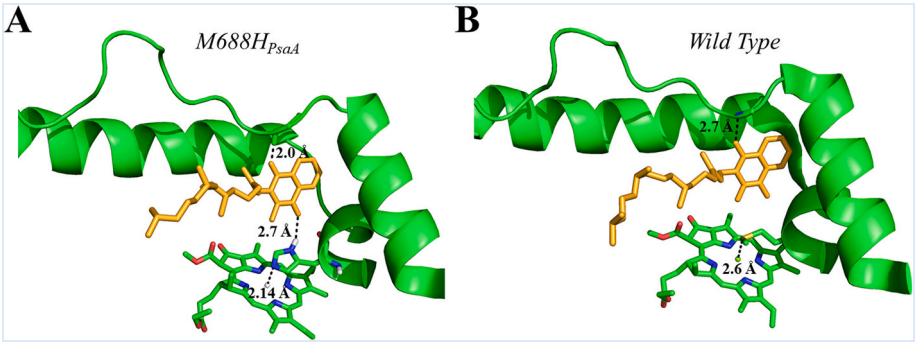

Fig. 3. The axial ligation of the Chl_{3A} molecule in (A) the $M688H_{PsaA}$ variant of PS I where the $M688_{PsaA}$ was replaced by a His residue, and (B) WT PS I [9].

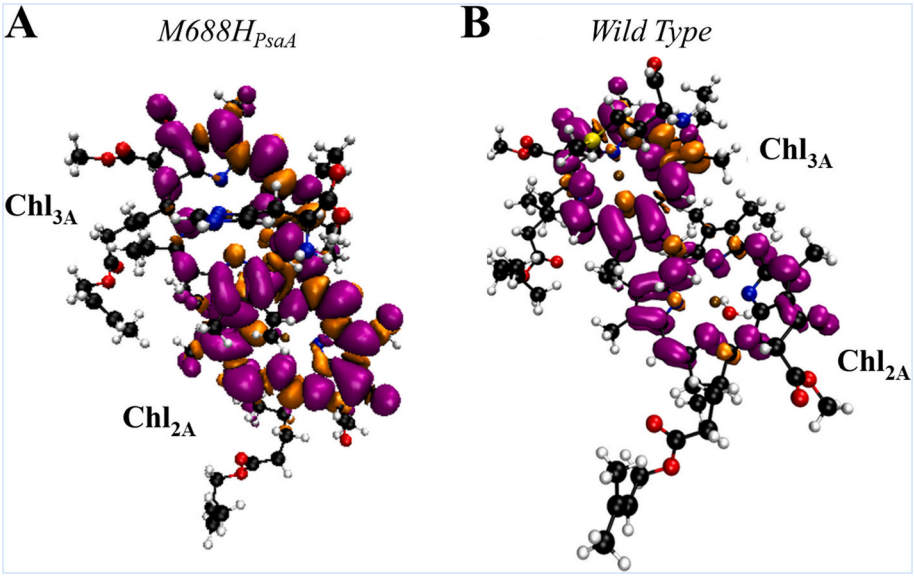

Fig. 4. Electron spin density distribution in the singly occupied molecular orbital (SOMO) of the $A_0^{\bullet-}$ state in a computational model containing the A_{1A}, Chl_{3A} and Chl_{2A} cofactors with the (A) $H688_{PsaA}$ and water molecule that are axially ligated to Chl_{3A} and Chl_{2A}, respectively, in the $M688H_{PsaA}$ variant of PS I with the numbering scheme that is employed to label the pyrrole groups of each Chl ring and (B) $M688_{PsaA}$ residue and water molecule that are axially ligated to Chl_{3A} and Chl_{2A}, respectively, in wild-type PS I.

peak in the (+,+) quadrant of the $M688H_{PsaA}$ spectrum that corresponds to the presence of a weakly hyperfine-coupled nitrogen atom, N^D. In determining the identity of the new spectral feature, we turned our attention to the quadrupolar coupling constant, K, that reflects the nature of the electric field gradient around a quadrupolar nucleus (where I > 1), such as a ^{14}N atom with a nuclear spin, I, of 1 (see [56,71] for a review). The value of K of 0.69 MHz for the $N^{A–C}$ atoms that were hyperfine coupled to the electron spin in the $A_{0A}^{\bullet-}$ state were identical to those obtained for the analogous ^{14}N atoms in the $A_0^{\bullet-}$ state in WT PS I, and correspond to the pyrrole nitrogen atoms of the Chl ring [28]. However, the value of K for N^D was 0.74 MHz, corresponding to an imino nitrogen of a histidine residue. DFT calculations provided further confirmation of the identity of N^D, as they revealed electron spin density on the ε-nitrogen of $H688_{PsaA}$, which is in close proximity to the central Mg^{2+} ion of the Chl_{3A} cofactor. Thus, both the experimental and computational studies indicate that the $H688_{PsaA}$ serves as an axial ligand to the Chl_{3A} cofactor.

Despite clear evidence of the coordination of the histidine residue, $H688_{PsaA}$, as an axial ligand at the central Mg^{2+} ion of the Chl_{3A} cofactor in this study and the significant impact on the rates of electron transfer observed previously [9], the impact on the delocalization of the electron spin density over the $Chl_{2A/2B}$ and $Chl_{3A/3B}$ cofactors in the $A_{0A}^{\bullet-}$ state of $M688H_{PsaA}$ PS I is minimal. The values of the isotropic hyperfine coupling, A_{iso}, for the hyperfine-coupled nitrogen atoms in the $A_0^{\bullet-}$ state of WT PS I range from 0.52–2.80 MHz [28], while the A_{iso} values of the $A_{0A}^{\bullet-}$ in the $M688H_{PsaA}$ variant of PS I with the $H688_{PsaA}$ residue coordinated to the central Mg^{2+} ion of the Chl_{3A} cofactor range from 0.57–2.80 MHz. This suggests that there is no change in the electron spin delocalization over the $Chl_{2A/2B}$ and $Chl_{3A/3B}$ cofactors in the $A_{0A}^{\bullet-}$ state of $M688H_{PsaA}$ PS I. Further, the identities of the specific pyrrole nitrogens that are involved in the delocalization of the electron spin density in the $A_0^{\bullet-}$ state remains unchanged (Fig. 4A). This suggests that the delocalization of the electron spin density in the $A_0^{\bullet-}$ state is robust and independent of the identity of the axial ligand that is coordinated to the central Mg^{2+} ion of the Chl_{3A} cofactor. Nevertheless, the DFT calculations reveal a change in the asymmetry of the delocalization over the $Chl_{2A/2B}$ and $Chl_{3A/3B}$ cofactors in the $A_{0A}^{\bullet-}$ state, shown in Fig. 4A–B. It appears that distribution over the Chl_{3A} and Chl_{2A} cofactors is asymmetric in favor of Chl_{3A} in the $A_0^{\bullet-}$ state of WT PS I, while the electron spin density distribution is in favor of the Chl_{2A} cofactor in the $M688H_{PsaA}$ variant of PS I.

Understanding the effects of the substitution of an axial ligand at the central Mg^{2+} ion on the redox potential of a Chl cofactor can help elucidate the effects that the replacement of $Met688_{PsaA}$ by a His residue has on the asymmetry of delocalization and electron transfer reactions within PS I. A previous theoretical study by Heimdal and coworkers [82] interrogated the effects of various axial ligands on the redox properties of monomeric Chls. Assuming a dielectric constant, ε, of 4 for a protein matrix [83,84], it was determined that the order from most oxidizing to most reducing axial ligands to the central Mg^{2+} ion are: No axial ligand (−1.69 V), Met (−1.79 V), Ser (−1.84 V), H_2O (−1.87 V), and His (−1.90 V). This suggests that the axial coordination of a His residue would result in a slight decrease in the redox potential of a Chl cofactor in comparison with an axial Met ligand. Moreover, in WT PS I, the Chl_{3A} cofactor is coordinated by an axial Met ligand, whereas Chl_{2A} is coordinated by a water molecule (Fig. 1B). The difference in the redox potentials would likely result in Chl_{2A} being ~80 mV more reducing than Chl_{3A}, which in turn would lead to a slight preference for the distribution of electron spin density to favor Chl_{3A} (Fig. 4B). In contrast, when the axial Met ligand of Chl_{3A} is replaced by a His residue, the difference in the redox potential between Chl_{3A} and Chl_{2A} is inverted, as Chl_{3A} would be ~30 mV more reducing than Chl_{2A}, which could result in a slight increase in the electron spin density distribution in favor of the Chl_{2A} cofactor. Thus, it appears that although the overall delocalization of the electron spin density over the Chl_{3A} and Chl_{2A} cofactors in the $A_0^{\bullet-}$ state is independent of the axial ligand to the central Mg^{2+} ion, the choice of the ligand may exert a slight influence on the relative distribution of this delocalization over the Chl dimer, which can, in turn, have a significant impact on electron transfer efficiency.

5. Conclusions

Using a combination of 2D HYSCORE spectroscopy and DFT calculations, we demonstrate that the His that replaces $M688_{PsaA}$ residue in the $M688H_{PsaA}$ variant of PS I serves as the axial ligand to the Chl_{3A} cofactor. Analysis of the quadrupolar coupling constant of the 2D HYSCORE signal from the hyperfine-coupled nitrogen atoms reveals that the imino nitrogen of a His residue is an axial ligand to the Chl_{3A} cofactor in the $A_{0A}^{\bullet-}$ state. Additionally, MD simulations confirm that the His has a preferential orientation toward the Mg^{2+}, and DFT calculations on this complex revealed that the previously discovered delocalization over the Chl_{2A}/Chl_{3A} dimer in the $A_{0A}^{\bullet-}$ state of the $M688H_{PsaA}$ variant of PS I is not disrupted by the His replacement, showing that the dimerization of Chl_2 and Chl_3 is independent of the identity of the axial ligand to the constituent Chl cofactors. However, there is an inversion of the asymmetry, now in favor of Chl_2, which may better explain the inhibition of forward

electron transfer to A_1 when A_0 is ligated by His. This work reveals that the choice of an axial ligand to the Chls is yet another factor that is employed in PS I to fine tune the electronic structure and redox properties of the donors and acceptors that are involved in the light-driven electron transfer pathway.

Declaration of competing interest

The authors declare that they have no known competing financial interests or personal relationships that could have appeared to influence the work reported in this paper.

Acknowledgments

This study is supported by the Photosynthetic Systems Program, Office of Basic Energy Sciences of the U.S. Department of Energy under the contract DE-FG02-07ER15903 (KVL) and DE-SC0010575 (JHG). The authors acknowledge support from the NSF REU Program in Physics (grant number 1560266) for EG and thank the Center for Computational Innovations at RPI for computational resources.

Appendix A. Supplementary data

Supplementary data to this article can be found online at https://doi.org/10.1016/j.bbabio.2021.148424.

References

[1] A. N. Webber, W. Lubitz, P_{700}: the primary electron donor of photosystem I. Biochim. Biophys. Acta Bioenerg. 1507, 61–79 (2001).
[2] J.H. Golbeck, Photosystem I: The Light-driven Plastocyanin: Ferredoxin Oxidoreductase, Springer, Dordrecht, 2006.
[3] P. Fromme, P. Jordan, N. Krauß, Structure of photosystem I. Biochim. Biophys. Acta Bioenerg. 1507, 5–31 (2001).
[4] P. Jordan, et al., Three-dimensional structure of cyanobacterial photosystem I at 2.5 A resolution, Nature 411 (2001) 909–917.
[5] G. Feher, J.P. Allen, M.Y. Okamura, D.C. Rees, Structure and function of bacterial photosynthetic reaction centres, Nature 339 (1989) 111–116.
[6] M.R. Gunner, The reaction center protein from purple bacteria: structure and function, Curr. Top. Bioenerg. 16 (1991) 319–367.
[7] S. Savikhin, R. Jankowiak, Mechanism of primary charge separation in photosynthetic reaction centers, in: J.H. Golbeck, A. van der Est (Eds.), The Biophysics of Photosynthesis, Springer, New York, NY, 2014, pp. 193–240, https://doi.org/10.1007/978-1-4939-1148-6_7.
[8] T.L. Olson, J.C. Williams, J.P. Allen, The three-dimensional structures of bacterial reaction centers, Photosyn Res 120 (2014) 87–98.
[9] J. Sun et al., Evidence that histidine forms a coordination bond to the A_{0A} and A_{0B} chlorophylls and a second H-bond to the A_{1A} and A_{1B} phylloquinones in M688HPsaA and M668HPsaB variants of *Synechocystis* sp. PCC 6803. Biochim Biophys Acta Bioenerg 1837, 1362–1375 (2014).
[10] H. Makita, G. Hastings, Directionality of electron transfer in cyanobacterial photosystem I at 298 and 77K, FEBS Lett. 589 (2015) 1412–1417.
[11] V. Kurashov et al., Critical evaluation of electron transfer kinetics in P_{700}-F_A/F_B, P_{700}-F_X, and P_{700}-A_1 photosystem I core complexes in liquid and in trehalose glass. Biochim. Biophys. Acta Bioenerg. 1859, 1288–1301 (2018).
[12] N. Srinivasan, J. H. Golbeck, Protein-cofactor interactions in bioenergetic complexes: the role of the A_{1A} and A_{1B} phylloquinones in photosystem I. Biochim. Biophys. Acta 1787, 1057–1088 (2009).
[13] N. Srinivasan, I. Karyagina, R. Bittl, A. van der Est, J. H. Golbeck, Role of the hydrogen bond from Leu722 to the A_{1A} phylloquinone in photosystem I. Biochemistry 48, 3315–3324 (2009).
[14] N. Srinivasan, et al., Alteration of the H-bond to the A_{1A} phylloquinone in photosystem I: influence on the kinetics and energetics of electron transfer, J. Phys. Chem. B 115 (2011) 1751–1759.
[15] N. Srinivasan, R. Chatterjee, S. Milikisiyants, J. H. Golbeck, K. V. Lakshmi, Effect of hydrogen bond strength on the redox properties of phylloquinones: a two-dimensional hyperfine sublevel correlation spectroscopy study of photosystem I. Biochemistry 50, 3495–3501 (2011).
[16] G. Milanovsky et al., Multiple pathways of charge recombination revealed by the temperature dependence of electron transfer kinetics in cyanobacterial photosystem I. Biochim. Biophys. Acta Bioenerg. 1860, 601–610 (2019).
[17] A. van der Est, et al., Incorporation of 2,3-disubstituted-1,4-naphthoquinones into the A_1 binding site of photosystem I studied by EPR and ENDOR spectroscopy, Appl Magn Res 37 (2009) 65.
[18] J. Fajer, et al., Primary electron acceptors in plant photosynthesis, J Amer Chem Soc 102 (1980) 7143–7145.
[19] A. Forman, et al., Mechanisms of energy transduction in plant photosynthesis: ESR, ENDOR and MOs of the primary acceptors, Isr J Chem 21 (1981) 265–269.
[20] V.A. Shuvalov, A.V. Klevanik, A.V. Sharkov, P.G. Kryukov, K.E. Bacon, Picosecond spectroscopy of photosystem I reaction centers, FEBS Lett. 107 (1979) 313–316.
[21] V. V. Ptushenko, D. A. Cherepanov, L. I. Krishtalik, A. Y. Semenov, Semi-continuum electrostatic calculations of redox potentials in photosystem I. Photosyn Res 97, 55 (2008).
[22] M.G. Müller, J. Niklas, W. Lubitz, A.R. Holzwarth, Ultrafast transient absorption studies on photosystem I reaction centers from *Chlamydomonas reinhardtii*. 1. a new interpretation of the energy trapping and early electron transfer steps in photosystem I, Biophys. J. 85 (2003) 3899–3922.
[23] O.G. Poluektov, S.V. Paschenko, L.M. Utschig, K.V. Lakshmi, M.C. Thurnauer, Bidirectional electron transfer in photosystem I: direct evidence from high-frequency time-resolved EPR spectroscopy, J Amer Chem Soc 127 (2005) 11910–11911.
[24] A. R. Holzwarth, M. G. Müller, J. Niklas, W. Lubitz, Ultrafast transient absorption studies on photosystem I reaction centers from *Chlamydomonas reinhardtii*. 2: mutations near the P_{700} reaction center chlorophylls provide new insight into the nature of the primary electron donor. Biophys. J. 90, 552–565 (2006).
[25] M.G. Müller, C. Slavov, R. Luthra, K.E. Redding, A.R. Holzwarth, Independent initiation of primary electron transfer in the two branches of the photosystem I reaction center, Proc. Natl. Acad. Sci. U. S. A. 107 (2010) 4123–4128.
[26] D.A. Cherepanov, et al., Generation of ion-radical chlorophyll states in the light-harvesting antenna and the reaction center of cyanobacterial photosystem I, Photosyn Res (2020), https://doi.org/10.1007/s11120-020-00731-0.
[27] D.A. Cherepanov, et al., Primary charge separation within the structurally symmetric tetrameric $Chl_{2A}P_AP_BChl_{2B}$ chlorophyll exciplex in photosystem I, J. Photochem. Photobiol. B 217 (2021), 112154.
[28] M. Gorka, Charles, P., Kalendra, V., Lakshmi, K.V., Golbeck, J.H., A dimeric chlorophyll electron acceptor differentiates type I from type II photosynthetic reaction centers iScience (manuscript in review) (2020).
[29] R.G. Pearson, Hard and soft acids and bases, J Amer Chem Soc 85 (1963) 3533–3539.
[30] I. V. Shelaev et al., Femtosecond primary charge separation in *Synechocystis* sp. PCC 6803 photosystem I. Biochim. Biophys. Acta 1797, 1410–1420 (2010).
[31] W. V. Fairclough et al., Bidirectional electron transfer in photosystem I: electron transfer on the PsaA side is not essential for phototrophic growth in Chlamydomonas. Biochim. Biophys. Acta Bioenerg. 1606, 43–55 (2003).
[32] V.M. Ramesh, K. Gibasiewicz, S. Lin, S.E. Bingham, A.N. Webber, Bidirectional electron transfer in photosystem I: accumulation of A_0^- in A-side or B-side mutants of the axial ligand to chlorophyll A_0, Biochemistry 43 (2004) 1369–1375.
[33] S. Santabarbara, et al., Bidirectional electron transfer in photosystem I: determination of two distances between P_{700}^+ and A_1^- in spin-correlated radical pairs, Biochemistry 44 (2005) 2119–2128.
[34] M. Byrdin et al., Assignment of a kinetic component to electron transfer between iron–sulfur clusters F_X and $F_{A/B}$ of photosystem I. Biochim. Biophys. Acta Bioenerg. 1757, 1529–1538 (2006).
[35] W. Giera, K. Gibasiewicz, V.M. Ramesh, S. Lin, A. Webber, Electron transfer from A^{-0} to A_1 in photosystem I from *Chlamydomonas reinhardtii* occurs in both the A and B branch with 25–30-ps lifetime, Phys. Chem. Chem. Phys. 11 (2009) 5186–5191.
[36] T. Berthold, et al., Exploring the electron transfer pathways in photosystem I by high-time-resolution electron paramagnetic resonance: observation of the B-side radical pair $P_{700}^+A_{1B}^-$ in whole cells of the deuterated green alga *Chlamydomonas reinhardtii* at cryogenic temperatures, J Amer Chem Soc 134 (2012) 5563–5576.
[37] R.O. Cohen, et al., Evidence for asymmetric electron transfer in cyanobacterial photosystem I: analysis of a methionine-to-leucine mutation of the ligand to the primary electron acceptor A_0, Biochemistry 43 (2004) 4741–4754.
[38] N. Dashdorj, W. Xu, R.O. Cohen, J.H. Golbeck, S. Savikhin, Asymmetric electron transfer in cyanobacterial photosystem I: charge separation and secondary electron transfer dynamics of mutations near the primary electron acceptor A_0, Biophys. J. 88 (2005) 1238–1249.
[39] A. Savitsky, et al., Alteration of the axial met ligand to electron acceptor A_0 in photosystem I: effect on the generation of $P_{700}^+A_1^-$ radical pairs as studied by W-band transient EPR, Appl. Magn. Reson. 37 (2009) 85.
[40] A. van der Est, et al., Alteration of the axial Met ligand to electron acceptor A_0 in photosystem I: an investigation of electron transfer at different temperatures by multifrequency time-resolved and CW EPR, Appl. Magn. Reson. 37 (2009) 103.
[41] S. Santabarbara, et al., Directionality of electron-transfer reactions in photosystem I of prokaryotes: universality of the bidirectional electron-transfer model, J. Phys. Chem. B 114 (2010) 15158–15171.
[42] K. Brettel, Electron transfer from A_1 to an iron-sulfur center with t = 200 ns at room temperature in photosystem I characterization by flash absorption spectroscopy, FEBS Lett. 239 (1988) 93–98.
[43] M. Mac, X.-S. Tang, B.A. Diner, J. McCracken, G.T. Babcock, Identification of histidine as an axial ligand to P_{700}^+Biochemistry 35 (1996) 13288–13293.
[44] M. Mac, N.R. Bowlby, G.T. Babcock, J. McCracken, Monomeric spin density distribution in the primary donor of photosystem I as determined by electron magnetic resonance: functional and thermodynamic implications, J Amer Chem Soc 120 (1998) 13215–13223.
[45] H. Käss, P. Fromme, H.T. Witt, W. Lubitz, Orientation and electronic structure of the primary donor radical cation in photosystem I: a single crystals EPR and ENDOR Study, J. Phys. Chem. B 105 (2001) 1225–1239.
[46] Y. Deligiannakis, A. W. Rutherford, Electron spin echo envelope modulation spectroscopy in photosystem I. Biochim. Biophys. Acta Bioenerg. 1507, 226–246 (2001).

[47] Y. Deligiannakis, J. Hanley, A.W. Rutherford, 1D- and 2D-ESEEM study of the semiquinone radical $Q_{\bar{A}}$ of photosystem II, J Amer Chem Soc 121 (1999) 7653–7664.
[48] W. Lubitz, F. Lendzian, R. Bittl, Radicals, radical pairs and triplet states in photosynthesis, Acc. Chem. Res. 35 (2002) 313–320.
[49] R. D. Britt et al., Recent pulsed EPR studies of the photosystem II oxygen-evolving complex: implications as to water oxidation mechanisms. Biochim. Biophys. Acta Bioenerg. 1655, 158–171 (2004).
[50] P. Charles, et al., Two-dimensional ^{67}Zn HYSCORE spectroscopy reveals that a Zn-bacteriochlorophyll a_P' dimer is the primary donor (P_{840}) in the type-1 reaction centers of *Chloracidobacterium thermophilum*, Phys. Chem. Chem. Phys. 22 (2020) 6457–6467.
[51] M. Rögner, P.J. Nixon, B.A. Diner, Purification and characterization of photosystem I and photosystem II core complexes from wild-type and phycocyanin-deficient strains of the cyanobacterium *Synechocystis* PCC 6803, J. Biol. Chem. 265 (1990) 6189–6196.
[52] S. Stoll, A. Schweiger, EasySpin, a comprehensive software package for spectral simulation and analysis in EPR, J. Magn. Reson. 178 (2006) 42–55.
[53] F. Neese, The ORCA program system, WIREs Comput Mol Sci 2 (2012) 73–78.
[54] F. Neese, Software update: the ORCA program system, version 4.0, WIREs Comput Mol Sci 8 (2018), e1327.
[55] W. Humphrey, A. Dalke, K. Schulten, VMD: Visual molecular dynamics, J. Mol. Graph. 14 (1996) 33–38.
[56] Y. Deligiannakis, M. Louloudi, N. Hadjiliadis, Electron spin echo envelope modulation (ESEEM) spectroscopy as a tool to investigate the coordination environment of metal centers, J. Coord. Chem. 204 (2000) 1–112.
[57] K.V. Lakshmi, G.W. Brudvig, Pulsed electron paramagnetic resonance methods for macromolecular structure determination, Curr. Opin. Struct. Biol. 11 (2001) 523–531.
[58] Thomas Prisner, F. MacMillan a. Martin Rohrer, Pulsed EPR spectroscopy: biological applications, Annu. Rev. Phys. Chem. 52 (2001) 279–313.
[59] G. Feher, Observation of nuclear magnetic resonances via the electron spin resonance line, Phys. Rev. 103 (1956) 834–835.
[60] W.B. Mims, Pulsed endor experiments. Proc R Soc Lond Proceedings of the Royal Society of London. Series A, Math Phys Sci 283 (1965) 452–457.
[61] E.R. Davies, A new pulse endor technique, Phys. Lett. A 47 (1974) 1–2.
[62] A. Schweiger, Jeschke, G., Principles of Pulse Electron Paramagnetic Resonance. (Oxford University Press, Oxford, 2001), vol. 79, pp. 103–103.
[63] S.A. Dikanov, Y. Tsvetkov, Electron Spin Echo Envelope Modulation (ESEEM) Spectroscopy, CRC press, 1992.
[64] P. Höfer, A. Grupp, H. Nebenführ, M. Mehring, Hyperfine sublevel correlation (HYSCORE) spectroscopy: a 2D ESR investigation of the squaric acid radical, Chem. Phys. Lett. 132 (1986) 279–282.
[65] R. Chatterjee, S. Milikisiyants, C.S. Coates, K.V. Lakshmi, High-resolution two-dimensional ^{1}H and ^{14}N hyperfine sublevel correlation spectroscopy of the primary quinone of photosystem II, Biochemistry 50 (2011) 491–501.
[66] S. Milikisiyants, et al., Ligand environment of the S2 state of photosystem II: a study of the hyperfine interactions of the tetranuclear manganese cluster by 2D ^{14}N HYSCORE spectroscopy, J. Phys. Chem. B 114 (2010) 10905–10911.
[67] R. Chatterjee, et al., The structure and activation of substrate water molecules in Sr^{2+}-substituted photosystem II, Phys. Chem. Chem. Phys. 16 (2014) 20834–20843.
[68] B. Mark, et al., Determining the electronic structure of paramagnetic intermediates in membrane proteins: a high-resolution 2D ^{1}H hyperfine sublevel correlation study of the redox-active tyrosines of photosystem II, Biochim Biophys Acta Biomembr 1862 (2020), 183422.
[69] I. García-Rubio, J.I. Martínez, R. Picorel, I. Yruela, P.J. Alonso, HYSCORE spectroscopy in the cytochrome b_{559} of the photosystem II reaction center, J Amer Chem Soc 125 (2003) 15846–15854.
[70] S. Van Doorslaer, Understanding heme proteins with hyperfine spectroscopy, J. Magn. Reson. 280 (2017) 79–88.
[71] D.T. Edmonds, Nuclear quadrupole double resonance, Phys. Rep. 29 (1977) 233–290.
[72] I. H. Davis, P. Heathcote, D. J. MacLachlan, M. C. W. Evans, Modulation analysis of the electron spin echo signals of *in vivo* oxidised primary donor ^{14}N chlorophyll centres in bacterial, P_{870} and P_{960}, and plant photosystem I, P_{700}, reaction centres. Biochim. Biophys. Acta Bioenerg. 1143, 183–189 (1993).
[73] H. Käβ, E. Bittersmann-Weidlich, L. E. Andréasson, B. Bönigk, W. Lubitz, ENDOR and ESEEM of the ^{15}N labelled radical cations of chlorophyll a and the primary donor P_{700} in photosystem I. Chem Phys 194, 419–432 (1995).
[74] A.J. Hoff, F. Lendzian, K. Möbius, W. Lubitz, Proton and nitrogen electron nuclear double and triple resonance of the chlorophyll a anion in liquid solution, Chem. Phys. Lett. 85 (1982) 3–8.
[75] S.E.J. Rigby, J.H.A. Nugent, P.J. O'Malley, ENDOR and special triple resonance studies of chlorophyll cation radicals in photosystem 2, Biochemistry 33 (1994) 10043–10050.
[76] P.J. O'Malley, Hybrid density functional studies of pheophytin anion radicals: implications for initial electron transfer in photosynthetic reaction centers, J. Phys. Chem. B 104 (2000) 2176–2182.
[77] A. Sirohiwal, F. Neese, D.A. Pantazis, Protein matrix control of reaction center excitation in photosystem II, J. Am. Chem. Soc. 142 (2020) 18174–18190.
[78] S. Stoll, C. Calle, G. Mitrikas, A. Schweiger, Peak suppression in ESEEM spectra of multinuclear spin systems, J. Magn. Reson. 177 (2005) 93–101.
[79] A.T. Taguchi, A. Baldansuren, S.A. Dikanov, Basic and combination cross-features in X- and Q-band HYSCORE of the ^{15}N labeled bacteriochlorophyll a cation radical, Z. Phys. Chem. 231 (2017) 725–743.
[80] P.K.K. Pandey, P. Chandra, Theoretical study of isotropic hyperfine coupling constants in small radicals by MINDO/3 method, Can. J. Chem. 57 (1979) 3126–3134.
[81] H. Käβ, W. Lubitz, Evaluation of 2D ESEEM data of ^{15}N-labeled radical cations of the primary donor P_{700} in photosystem I and chlorophyll a, Chem. Phys. Lett. 251 (1996) 193–203.
[82] J. Heimdal, K.P. Jensen, A. Devarajan, U. Ryde, The role of axial ligands for the structure and function of chlorophylls, J. Biol. Inorg. Chem. 12 (2007) 49–61.
[83] B. Honig, A. Nicholls, Classical electrostatics in biology and chemistry, Science 268 (1995) 1144–1149.
[84] K.A. Sharp, B. Honig, Electrostatic interactions in macromolecules: theory and applications, Annu. Rev. Biophys. Biophys. Chem. 19 (1990) 301–332.